White Rose
university consortium
Universities of Leeds, Sheffield & York

eprints@whiterose.ac.uk
https://eprints.whiterose.ac.uk/

Streamwise Pressure Gradient Effect on Görtler Vortices: a Numerical Study in the Compressible Regime

Omar Es-Sahli[1], Adrian Sescu[1], Zamir Koshuriyan[2], Yuji Hattori[3]
[1] Mississippi State University, Mississippi State, MS, USA 39762.
[2] University of York, United Kingdom
[3] Institute of Fluid Science, Tohoku University, Sendai, 980-8577, Japan

ABSTRACT

We investigate the influence of streamwise pressure gradient on the Görtler vortex system initiation and development in high-speed compressible boundary layers. We conduct a parametric study in which we vary the pressure gradient in a supersonic flow at Mach number 3. Preliminary results include velocity and temperature plots, vortex energy distributions, and velocity profiles.

1. Introduction

Streaks formation in pre-transitional boundary layer flows over flat or curved surfaces occur when the height of roughness elements exceeds a critical value (e.g., White [1], Goldstein et al. [2], Wu & Choudhari [3]), or when the amplitude of the freestream disturbances exceeds a given threshold (e.g., Kendall [4], Westin et al. [5], Goldstein & Sescu [6]). The velocity component in the streamwise direction exhibits elongated 'streaky' features, characterized by adjacent regions of acceleration (high-speed) and deceleration (low-speed) of fluid particles (e.g., Kendall [4] or Landahl [7]). In boundary layer flow along a concave surface, streaks of counter-rotating streamwise vortices form as a result of the imbalance between radial pressure gradients posed by the wall and centrifugal forces (e.g., Görtler [8], Hall [9], Swearingen & Blackwelder [10], or Sescu et al. [11]). The growth rate of these vortices depends on the surface curvature and the receptivity of the boundary layer to environmental disturbances and surface imperfections. Vortex formation can significantly alter the mean flow forcing the laminar flow to break down into turbulence.

In the compressible regime, researchers conducted a number of experimental studies to establish the gross correlation between the transition Reynolds number and freestream turbulence (FST) level. They showed that the transition position shifts significantly depending on both FST level (Dryden [12], Schneider [13]) and the surface roughness (Pate [14]). However, only few investigations of the detailed physics underlying such correlation exist. The experiments of Kendall [15] provide much information concerning supersonic boundary-layer transition under the influence of a high FST level. A salient feature is that fluctuations over a wide frequency range experience substantial growth within the boundary layer. Sufficiently downstream, a spectral peak emerges, which corresponds to the Mack-I mode in the low-Mach-number supersonic range ($M < 4.5$) (Mack [16]). For $M > 4.5$, a secondary, less pronounced peak representing the Mack-II instability appears. These results indicate that some kind of receptivity mechanism operates to generate instability waves in a nominally flat plate.

This paper explores the impact of streamwise pressure gradients on Görtler vortices in high-speed compressible boundary layers. It analyzes the development of streaks and vortices under adverse or favorable pressure gradients using various measurements and contour plots.

1.1 Governing Equations

In conservative form, the filtered Navier-Stokes equations are written as

$$\mathbf{Q}_t + \mathbf{F}_\xi + \mathbf{G}_\eta + \mathbf{H}_\zeta = \mathbf{S}. \tag{1}$$

where subscripts denote derivatives, the vector of conservative variables is given by

$$\mathbf{Q} = \frac{1}{J}\{\ \rho, \quad \rho u_i, \quad E\ \}^T, i = 1, 2, 3 \tag{2}$$

where J is the Jacobian, ρ is the non-dimensional density of the fluid, $u_i = (u, v, w)$ is the non-dimensional velocity vector in physical space, and E is the total energy. The flux vectors, $\mathbf{F}$, $\mathbf{G}$ and $\mathbf{H}$, are given by

$$\mathbf{F} = \frac{1}{J}\left\{\rho U, \rho u_i U + \xi_{x_i}(p + \tau_{i1}), EU + p\tilde{U} + \xi_{x_i}\Theta_i\right\}^T,$$

$$\mathbf{G} = \frac{1}{J}\left\{\rho V, \rho u_i V + \eta_{x_i}(p + \tau_{i2}), EV + p\tilde{V} + \eta_{x_i}\Theta_i\right\}^T,$$

$$\mathbf{H} = \frac{1}{J}\left\{\rho W, \rho u_i W + \zeta_{x_i}(p + \tau_{i3}), EW + p\tilde{W} + \zeta_{x_i}\Theta_i\right\}^T$$

where the contravariant velocity components are given by

$$U = \xi_{x_i}u_i, \quad V = \eta_{x_i}u_i, \quad W = \zeta_{x_i}u_i \tag{3}$$

with the Einstein summation convention applied over $i = 1, 2, 3$, the shear stress tensor and the heat flux are respectively given as

$$\tau_{ij} = \frac{\mu}{Re}\left[\left(\frac{\partial \xi_k}{\partial x_j}\frac{\partial u_i}{\partial \xi_k} + \frac{\partial \xi_k}{\partial x_i}\frac{\partial u_j}{\partial \xi_k}\right) - \frac{2}{3}\delta_{ij}\frac{\partial \xi_l}{\partial x_k}\frac{\partial u_k}{\partial \xi_l}\right] \tag{4}$$

$$\Theta_i = u_j\tau_{ij} + \frac{\mu}{(\gamma-1)M_\infty^2 RePr}\frac{\partial \xi_l}{\partial x_i}\frac{\partial T}{\partial \xi_l} \tag{5}$$

Corresponding author: Adrian Sescu
E-mail address: sescu@ae.msstate.edu

S is the source vector term, and μ is the dynamic viscosity.

The pressure p, the temperature T, and the density of the fluid are combined in the equation of state, $p = \rho T/\gamma M_\infty^2$. The Jacobian of the curvilinear transformation from the physical space to computational space is denoted by J. The derivatives ξ_x, ξ_y, ξ_z, η_x, η_y, η_z, ζ_x, ζ_y, and ζ_z represent grid metrics. The dynamic viscosity is linked to the temperature using Sutherland's equation in dimensionless form,

$$\mu = T^{3/2}\frac{1+C_1/T_\infty}{T+C_1/T_\infty}, \qquad (6)$$

while the thermal conductivity k is obtained from the Prandtl number, where for air at sea level, $C_1 = 110.4K$. There are no subgrid scale terms in equation (1) since an implicit large eddy simulation framework is considered here.

1.2 Numerical Algorithm

The compressible Navier-Stokes equations are solved in the framework of implicit large eddy simulations, where numerical filtering is applied to account for the missing sub-grid scale energy. The numerical algorithm uses high-order finite difference approximations for the spatial derivatives and explicit time marching. The time integration is performed using a third-order TVD Runge-Kutta method (Shu and Osher [17]). written in the form

$$
\begin{aligned}
\mathbf{Q}^{(0)} &= \mathbf{Q}^n \\
\mathbf{Q}^{(1)} &= \mathbf{Q}^{(0)} + \Delta t L(u^{(0)}) \\
\mathbf{Q}^{(2)} &= \frac{3}{4}\mathbf{Q}^{(0)} + \frac{1}{4}\mathbf{Q}^{(1)} + \frac{1}{4}\Delta t L(\mathbf{Q}^{(1)}) \quad (7) \\
\mathbf{Q}^{n+1} &= \frac{1}{3}\mathbf{Q}^{(0)} + \frac{2}{3}\mathbf{Q}^{(1)} + \frac{2}{3}\Delta t L(\mathbf{Q}^{(2)}),
\end{aligned}
$$

where $L(\mathbf{Q})$ is the residual.

The spatial derivatives are discretized using the dispersion-relation-preserving schemes of Tam and Webb [18] or a high-resolution 9-point dispersion-relation-preserving optimized scheme of Bogey et al. [19]. The first derivative at the lth node is approximated using M values of f to the right and N values of f to the left of the node.

$$\left(\frac{\partial f}{\partial x}\right)_l \simeq \frac{1}{\Delta x}\sum_{j=-N}^{M} a_j f_{l+j} \qquad (8)$$

By taking the Fourier transform of the above equation, the coefficients a_j are found by minimizing the integrated error of the difference between the wavenumber of the finite difference scheme and the wavenumber of the Fourier transform of the finite difference scheme.

2. Results

In figure 1, the mesh consisting of roughly 2 million grid points is displayed (every other mesh point is shown in all directions). The mesh is
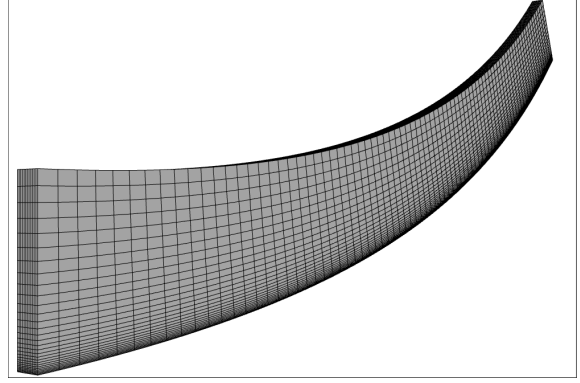

Fig. 1 Mesh used for the simulations (every other mesh point is shown in all directions).
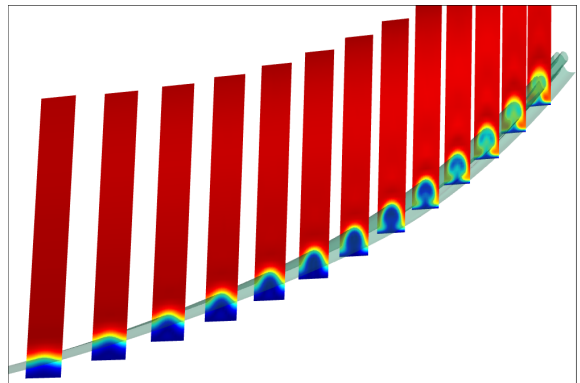

Fig. 2 Contour plots of the streamwise velocity in different crossflow planes).

clustered at the wall and stretched towards the upper boundary. No slip boundary condition for velocity and either adiabatic or isothermal condition for temperature is imposed at the wall. We impose vanishing gradients at the top and outflow boundaries and periodic conditions along the spanwise direction since we only simulate two streamwise counter-rotating vortices (corresponding to one mushroom shape). A transpiration condition imposes the streamwise pressure gradient on the top boundary.

Figure 2 shows velocity contour plots in the streamwise direction. The contour plots visually illustrate the growth of the centrifugal instabilities along the curved surface. The upstream perturbations trigger the counter-rotating vortices that gradually accelerate moving downstream. The high-velocity streaks result in faster flow circulations. This increase in angular velocity is seen visually as an increase in the amplitude of the mushroom structures.

Figure 3 illustrates the velocity contours of a single crossflow plane mushroom-like structure plotted at the same streamwise coordinate for three pressure gradient conditions; zero, favorable, and adverse. The simulation setup and freestream conditions are the same for all three cases. In terms of the amplitude of the mushroom-like structure,
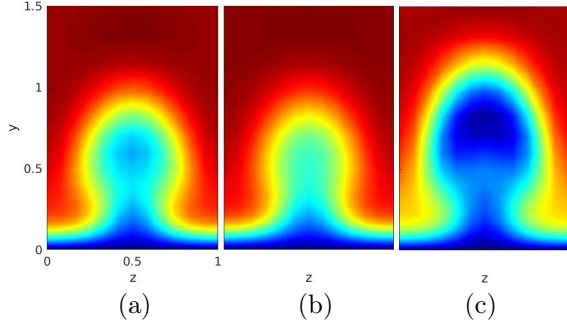
Fig. 3 Contours of streamwise velocity at a certain location: a) zero pressure gradient; b) favorable pressure gradient; c) adverse pressure gradient.

a qualitative assessment of the plots indicates that the adverse pressure gradient case results in the highest amplitude, followed by the zero gradient case resulting in medium size structures, then the favorable pressure gradient case, which results in the lowest amplitude. On the other hand, a close examination of the velocity magnitude inside the mushroom-like structures indicates that the flow is fastest for the favorable pressure gradient case, followed by the zero pressure gradient case resulting in slower streamwise velocity flow particles, then the adverse case where the flow velocity is almost negligible.

To put these observations in perspective, we examine the velocity profiles in the wall-normal direction along the center of the mushroom-like structure for the three pressure gradient cases, as shown in figure 4a. We start by looking at the zero pressure gradient case to set a reference for the other two cases. In this case, the boundary layer flow experiences the inherent adverse pressure gradient due to the surface curvature, which decreases its velocity. From this point, imposing the adverse pressure gradient condition adds to the inherent effects due to the surface curvature and causes the velocity of the flow to decrease further. On the other hand, imposing a favorable pressure gradient counteracts the inherent adverse pressure gradient, and the flow velocity decreases at a lower rate. The velocity profiles between the mushroom-like structures in figure 4b do not indicate significant disparities between the three cases.

Figure 5 shows the vortex kinetic energy distribution in the streamwise direction. The adverse pressure gradient case results in the highest energy level compared to the other two cases. Also, the energy starts picking up at an earlier streamwise location and has a higher growth rate than the zero and favorable pressure gradient cases. The zero pressure gradient case results in the second highest energy level, while the favorable pressure gradient case results in the lowest kinetic energy level, almost half that of the adverse pressure gradient case. On the other hand, the flow under the favorable pressure gradient condition reaches energy saturation first, followed by the zero pressure gradient and the adverse pressure gradient cases, respectively.
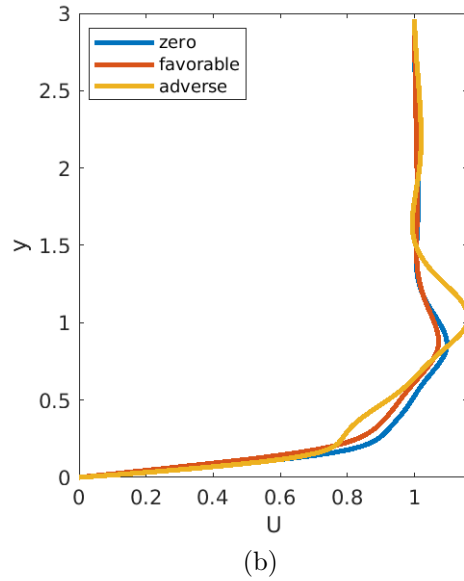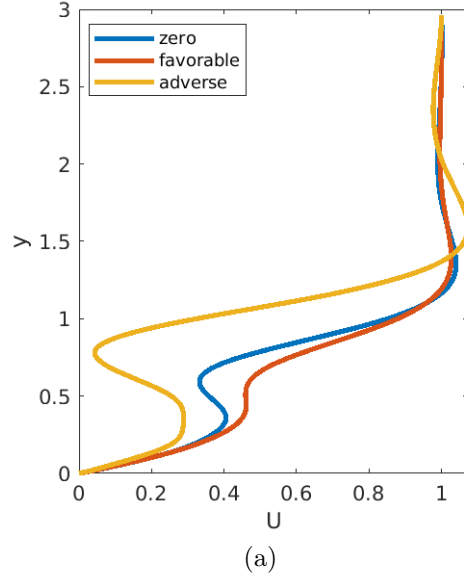

(a)

(b)

Fig. 4 Wall-normal profiles of streamwise velocity: a) between mushroom shapes; b) in the center of the mushroom.

Figure 6 shows the spanwise averaged wall shear stress for the three pressure gradient cases. The adverse pressure gradient case shows the highest drop in the wall shear stress. The decrease in the wall shear stress initiates at an earlier streamwise location and a steeper slope compared to the other pressure gradient cases. There is a subtle decrease in the zero pressure gradient case, while the wall shear stress follows a positive growth rate in the favorable pressure gradient case. Alike the pattern of figure 5, the flow under the favorable pressure gradient condition reaches saturation first, followed by the zero pressure gradient and the adverse pressure gradient cases, respectively.
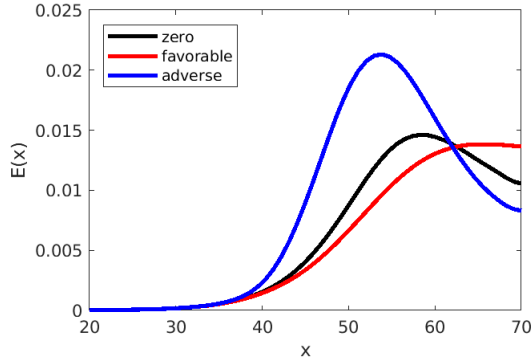
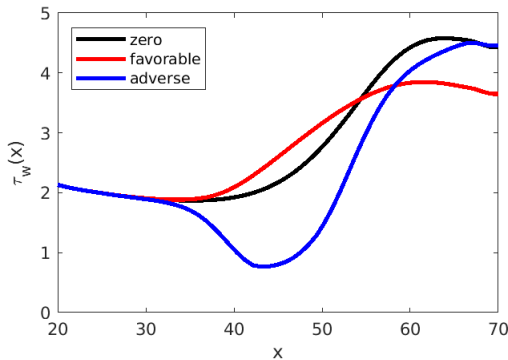Fig. 5 Vortex energy distribution in the streamwise direction.

Fig. 6 Wall shear stress distribution in the streamwise direction.

3. Conclusion

This paper presents the findings of a simulation study investigating fluid flow over a curved surface. The results reveal the formation and evolution of counter-rotating vortices, which are initiated by upstream perturbations and gain momentum downstream due to high-velocity streaks. The analysis of velocity contours and profiles sheds light on the impact of different pressure gradient conditions on the size and velocity of mushroom-like structures. Specifically, the adverse pressure gradient case exhibits larger structures but significantly lower flow velocity, while the favorable gradient case shows the opposite trend. The distribution of vortex kinetic energy and wall shear stress confirms these observations, with the adverse gradient case displaying the highest energy level and the most pronounced decrease in wall shear stress. These findings contribute to a deeper understanding of fluid flow dynamics and have potential implications for the optimization and design of curved surfaces in various engineering applications.

References

[1] White, E.B., *Phys. Fluids*, 14, (2002), 4429-4439.

[2] Goldstein, M., Sescu, A., Duck, P. and Choudhari, M., *Journal of Fluid Mechanics*, 644, (2010), 123-163.

[3] Wu, X. and Choudhari, M., *J. Fluid Mech.*, 483, (2011), 249-286.

[4] Kendall, J.M., *36th AIAA Aerospace Sciences Meeting and Exhibit*, (1998).

[5] Westin, K.J.A., Boiko, A.V., Klingmann, B.J.B., Kozlov, V.V. & Alfredsson, P.H., *J. Fluid Mech.*, 281, (1994), 193-218.

[6] Goldstein, M. & Sescu, *J. Fluid Mech.*, 613, (2008), 95-124.

[7] Landahl, M.T., *J. Fluid Mech.*, 98, (1980), 243-251.

[8] Görtler, H ., *ZAMM*, 21, (1941), 250–52; English version: *NACA Report 1375*, (1954)

[9] Hall, P., *Journal of Fluid Mechanics*, 124, (1982), 475-494.

[10] Swearingen, J.D. and Blackwelder, R.F., *J. Fluid Mech.*, 182, (1987), 255-290.

[11] Sescu, A. and Thompson, D., *Theoretical and Computational Fluids Dynamics*, 29, (2015), 67-92.

[12] Dryden, H. L., *Conference on High-Speed Aeronautics*, 41, (1955)

[13] Schneider, S. P., *J. Sp. Rock.*, 38-3, (2001), 323-333.

[14] Pate, S. R., *AIAA J.*, 9, (1971), 797-803.

[15] Kendall, J., *AIAA J.* 13, (1975), 290-299.

[16] Mack, L., *AIAA J.*, 3, (1975), 278-289.

[17] Shu, C.-W. and Osher, S., *Journal of Computational Physics* 77, No. 2, (1988), 439-471.

[18] Tam, C.K.W. and Webb, J.C., *Journal of Computational Physics*, 107, (1993) 262-281.

[19] Bogey, C. and Bailly, C., *Journal of Computational Physics*, 194, (2004), 194-214.